ASME Journal of Engineering for Gas Turbines and Power
Online journal at:
https://asmedigitalcollection.asme.org/gasturbinespower

Edoardo Gheller[1]
Department of Mechanical Engineering,
Politecnico di Milano,
Milan 20156, Italy
e-mail: edoardo.gheller@polimi.it

Vishnu Vardhan Reddy
Baker Hughes,
Hyderabad 500081, India
e-mail: vishnuvardhan.reddy@bakerhughes.com

Satish Koyyalamudi
Baker Hughes,
Bangalore 560048, India
e-mail: Satish.K@bakerhughes.com

Steven Chatterton
Department of Mechanical Engineering,
Politecnico di Milano,
Milan 20156, Italy
e-mail: steven.chatterton@polimi.it

Daniele Panara
Baker Hughes,
Firenze 50129, Italy
e-mail: daniele.panara@bakerhughes.com

Paolo Pennacchi
Department of Mechanical Engineering,
Politecnico di Milano,
Milan 20156, Italy
e-mail: paolo.pennacchi@polimi.it

Tilting Pad Journal Bearing Computational Fluid Dynamic Parametric Modeling for New Energy Transition Challenges

The necessity of increasing the efficiency and reducing the carbon foot-print of machines is pushing centrifugal compressor bearings design to higher and higher peripheral speed and lower oil consumptions especially in the new energy transition fields, resulting in an increase in the bearing temperatures. Therefore, the bearing thermal management starts to play a major role in extending the machine operability and reducing the maintenance frequency. A full three-dimensional (3D) parametric conjugate heat transfer computational fluid dynamic (CFD) model for tilting pad journal bearings (TPJBs) is introduced in this paper to address the temperature aspects of oil-film bearings. The parametric geometry of the model and the automatic mesh update, allow the equilibrium position search to be obtained without adopting any dynamic mesh algorithms. The tilting pad and rotating shaft equilibrium position are automatically calculated with a Newton–Raphson algorithm. The static performance of the TPJB is investigated for different journal diameters, bearing clearance, and operating conditions. The numerical results obtained are compared with experimental data from compressor mechanical running tests to demonstrate the reliability of the model presented. The 3D distributions of the oil pressure, velocity, and temperature given by the CFD model, can be locally optimized to face the new energy transition challenges.
[DOI: 10.1115/1.4063831]

Keywords: tilting pad journal bearings, computational fluid dynamics, equilibrium position, lubrication, tribology, thermal model

1 Introduction

Fluid film bearing are widely used in industrial and energy sectors. Depending on the application, the machine size, rotating speed, and load transmitted to the bearing may change significantly as well as the bearing dynamic behavior. Understanding the lubricant hydrodynamic flow and thermal behavior of the bearings for different operating conditions is fundamental to have high fidelity, cost-effective, and robust rotordynamic designs that guarantee safe operations.

The most frequent approach followed for the modeling of tilting pad journal bearings (TPJBs) is based on the Reynolds equation. In 1964, Lund [1] presented a method to solve the isoviscous Reynolds equation to evaluate the frequency reduced force coefficients. In 1973, Tieu [2] developed a finite element model to solve the energy equation in infinitely long bearings considering the effect of the temperature on the oil viscosity. In 1988, Knight and Barrett developed a one-dimensional thermal hydrodynamic model of TPJBs considering the one-dimensional energy and Reynolds equation [3]. In 1994, Kim et al. [4] considered the pivot flexibility together with the shaft and pads distortions to develop a thermo-elastic hydrodynamic model applying a generalized Reynolds equation and two-dimensional energy equation. A complete three-dimensional (3D) modeling of TPJBs was presented by Suh and Palazzolo in 2015 [5]. The authors applied a generalized Reynolds equation, the 3D energy equation for the fluid film, and they considered the shaft, the pad, and the pivot flexibilities.

For the Reynolds equation modeling, the most critical aspect is assigning the temperature boundary condition at the leading edge of the pads. As a matter of fact, the whole temperature distribution in the oil film strongly depends on the temperature distribution assigned at the leading edge of the pad. Therefore, the whole static and dynamic properties and of the TPJBs are sensible to nonoptimal boundary condition assignment. The temperature distribution at each pad leading edge depends on the thermal balance occurring between the hot oil flowrate exiting from the previous pad, the mixing with the fresh oil coming from the supply circuit, and the oil leakage exiting from the sides. In Ref. [5], the inlet temperature of each pad is obtained from the energy balance between the cold oil entering in the bearing, the hot oil coming from the previous pad, and the oil entering the next pad, whereas the effect of oil leakage is not

Turbomachinery Technical Conference & Exposition, Hynes Convention Center, June 26–30, 2023. Turbo Expo 2023.
[1]Corresponding author.
Manuscript received August 2, 2023; final manuscript received August 24, 2023; published online December 26, 2023. Editor: Jerzy T. Sawicki.

considered. A mixing coefficient is introduced to guarantee physical results. A similar approach was adopted also in Ref. [6] and improved in Ref. [7] where the flowrate of oil leaked from the sides is considered in the thermal balance. Generally, the estimation of the inlet temperature is strongly affected by the mixing coefficient considered and only a constant temperature axial distribution can be obtained. To overcome this issue, Yang and Palazzolo built a machine learning tool able to predict the axial variation of the mixing coefficient [8]. The training dataset is built with the 3D computational fluid dynamic (CFD) model presented in Ref. [9]. As a further step, the authors proposed a convolutional auto-encoder that, depending on the operating conditions of the bearing, gives as output the bidimensional distribution of the temperature at the pad leading edge [10].

Considering the importance of the estimation of the mixing coefficient, the application of CFD in the modeling of TPJBs can result in better accuracy. Moreover, CFD modeling can treat the transition between laminar and turbulence lubrication [11].

The earliest TPJBs CFD models are simplified two-dimensional approaches [12,13]. A full 3D thermo-elastic hydrodynamic CFD model is proposed by Yang and Palazzolo in Refs. [14] and [15]. In Ref. [9], the authors improved the model including the pad flexibility. The equilibrium position is searched with a Newton–Raphson algorithm and a mesh deformation algorithm is adopted. Mesh deformation algorithms like the one proposed in Ref. [16] can be considered. However, the control on the mesh quality results difficult.

In this work, a 3D thermal hydrodynamic CFD model for TPJBs static performance is presented. The elastic behavior of the pad, shaft, and pivots is not considered since we are evaluating steady-state performance and the bearing load and speed are relatively low to comply with this hypothesis. Moreover, according to Ref. [17], the effect of the pivot flexibility strongly affects the dynamic force coefficients. While for low shaft speeds and bearing loads the effect on the static performances like temperatures and eccentricity is limited. The heat exchange between the pads and the oil is considered and the different thermal properties of the white metal overlay and base metal are also considered. The equilibrium position is found with a Newton–Raphson algorithm. The geometry is fully parametric and allows to evaluate bearings with different geometric characteristics and can be modified during the equilibrium search. Therefore, instead of applying a dynamic mesh deformation algorithm, an automatic remeshing algorithm is developed. The numerical results obtained are compared with experimental results obtained during mechanical running tests.

2 Materials and Methods

A family of flooded rocker back TPJB is considered in this study, see Fig. 1. In flooded bearing, the whole bearing housing is filled by oil and the flow is controlled by the tight clearance between the shaft and the bearing end seals. The end seals clearance depends on the shaft and end seals plates machining tolerances.

The main geometrical and operating parameters that characterize the bearing family are listed in Table 1. The five pad bearing family is designed with the possibility to choose between two clearance ranges: the reduced and the large clearance range. The reduced clearance range has an average assembly clearance around 1.1–1.2 [0/00], whereas the large clearance range has an average assembly clearance around 1.4–1.5 [0/00]. The bearing average preload is around 0.55 and the pad offset is 60%.

The pad temperature is monitored by thermal probes, typically thermos-resistances, located on the most loaded pads in the pad holes as shown in Fig. 2.

2.1 Computational Fluid Dynamic Model Architecture. The five bearing pads can freely adjust their angular position with respect to the practically fixed line of contact between the pad pivot and the bearing housing (see Fig. 3). The shaft position is also not fixed, and the equilibrium is reached when the sum of the pad oil-film forces counteracts the applied shaft load. Apart from operating parameters such as load, shaft speed, oil supply fluid pressure and temperature, pad angles, and shaft positions shall be iteratively determined to fulfill equilibrium. This assumes pads and shaft as a rigid body and pad pivot points as infinite stiffness. The pad pressure distribution and oil temperature are highly sensitive to pad angles and shaft position. For this reason, to obtain accurate bearing operating performance predictions, it is of paramount importance to obtain accurate pad equilibrium positions in CFD simulations.

Commercial CFD modeling and analysis tools from ANSYS and geometry manipulation tool Unigraphics have been used in the autonomous CFD analysis process developed. The architecture of the model is shown in Fig. 4. The user can visualize all the inputs and output parameters of an analysis through parameter set shown in Fig. 4. Geometric input parameters like bearing diameter, pad angles, rotor eccentricity, pad dimensions, bearing housing dimensions, and analysis input parameters like pressures and temperatures at inlet and outlet, rotor speed, and number of CFX

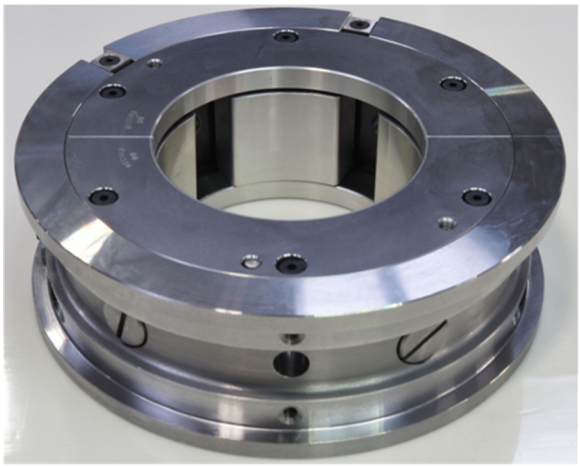

Fig. 1 TPJB considered in the analysis

Table 1 Geometrical and operating parameters of bearing family

Parameter	Value
Diameter	80 – 200 mm
Clearance range	Reduced, large
L/*D* ratio	0.44, 0.7
Load configuration	LOP, LBP
Oil type	ISO VG 32, ISO VG 46
Inlet pressure	0.3 – 2 barG
Inlet temperature	40 – 55 °C
Specific load	0.3 – 1.5 MPa
Shaft speed	3000 rpm – 75 m/s

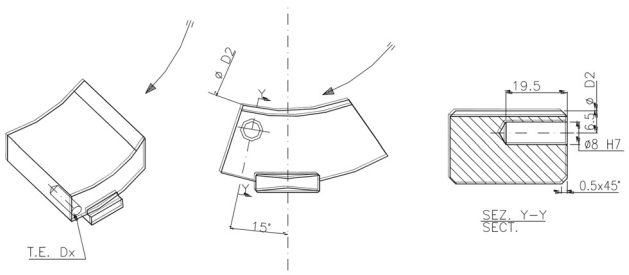

Fig. 2 Pad temperature probe layout

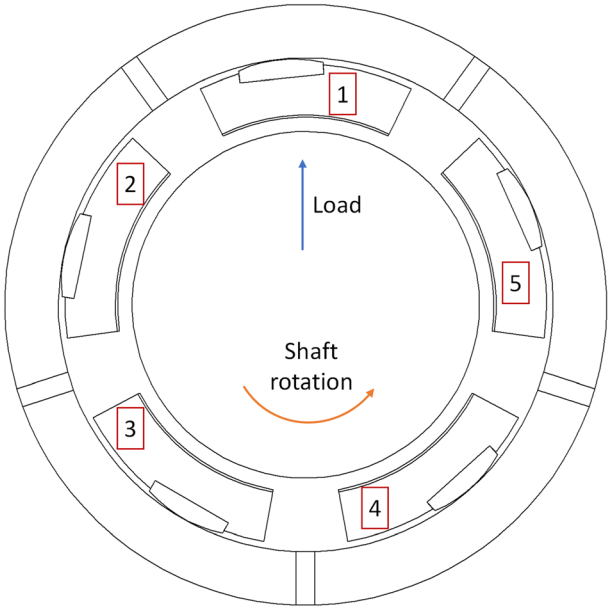

Fig. 3 Illustration of tilting pad journal bearing

iterations are varied from this parametric set. Also user selected list of parameters at each application like in ICEM the mesh quality and from CFX post-torque on each of the pads, power, temperature at selected locations can be seen in output parameters section of parameter set. User can change any of these input parameters, run the analysis and see the resultant outputs from this parametric set, without opening the applications.

Unigraphics is connected to ANSYS design modeler tool. The geometrical model is built parametrically so that the geometry can be automatically updated when the equilibrium position of the system is changed and when a bearing of a different size is investigated. Unique names are given to each geometric entity (edges, faces, and solids) such that the required entities are identified using these names by other tools in the process. This is one time process. Later the geometry is imported into ANSYS design modeler tool. When there is change in geometric or pads equilibrium parameters design modeler interacts with Unigraphics in background and performs necessary geometric updates.

ICEM CFD is used for meshing due to its ability to create complex computational grids and ease of programmability. ICEM CFD uses tool command language (TCL), a string-based programing language. The geometry from UG is transferred to ICEM CFD for the mesh generation. A TCL scrip is developed to generate hexahedral grid. The meshing script uses geometry parameters for parametric blocking, and for element size and distribution settings to customize the grid for given bearing size. The mesh specifications are assigned to the named selections defined in the geometry. A sample grid generated in this process is shown in Fig. 5, where due to the symmetry, only half of the bearing is considered. Across all bearing sizes a similar mesh quality is obtained. Few of the quality

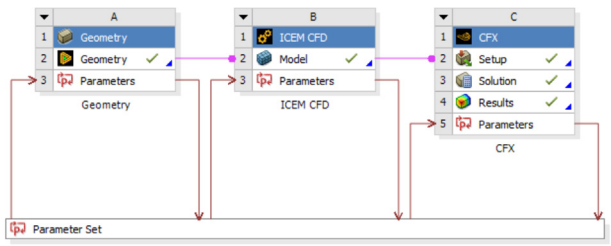

Fig. 4 CFD model architecture

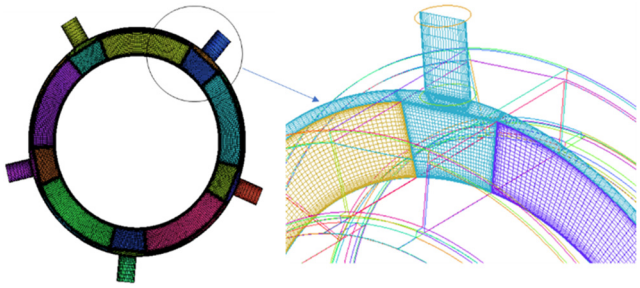

Fig. 5 Hexahedra grid using ICEM CFD tool

parameters checked to ensure mesh quality in ICEM are "Determinant > 0.3, Distortion > 0.5, and Quality > 0.3." Aspect ratio is high in thin film region but increases in the main film region. $Y+$ adjacent to the shaft walls is less than 0.5, while away from rotating regions average $Y+$ is less than 2.

The TCL script and the definition of the named selections allow to automatically update the mesh when the geometry of the TPJB is changed. Therefore, during the equilibrium position search the use of a mesh deformation algorithm is not necessary. With a mesh deformation algorithm, vast regions of the mesh are deformed. It is more difficult to maintain a constant mesh quality throughout the equilibrium calculation. On the contrary, with the proposed strategy a new mesh is computed at every equilibrium search iteration and the TCL script guarantees the same mesh quality at every step. Moreover, is a mesh deformation algorithm is applied, the equations governing the mesh deformation are solved, increasing the computation time. The new mesh calculation time is negligible with respect to the overall simulation time.

ANSYS CFX is selected as solver. The mesh is imported from the ICEM CFD block. In CFX-pre the boundary conditions are assigned. The main boundary conditions defined are shown in Fig. 6. All the boundary conditions are defined as parametric values. At inlet, total pressure and static temperatures are defined. At outlet, opening boundary type is used with opening pressures and opening temperatures defined. These opening pressure and temperatures are used in case, there is flow reversal at outlet boundary. Fluid–Solid interface are defined between oil and pad faces (five faces of each pad) with conservative interface heat flux option enabled. Solver uses conjugate heat transfer approach to match fluid and solid temperature and heat flux at the interfaces. The sixth face is defined as a symmetric boundary condition, as only half of the bearing is modeled. Both fluid and solid domains are simulated as stator and speed of rotating wall is specified, and no slip boundary condition is enabled. The faces of fluid domain adjacent to casing and the shaft surface are simulated as adiabatic. The inlet temperature, pressure, and rotor speed boundary conditions used for below analysis are from test measurements. The outlet pressure is set to experimental drain pressure (close to ambient pressure). Opening outlet temperature is set sump temperature. However, no reverse flow has been observed across all the bearing sizes, making this outlet opening temperature redundant. Working fluid is either "ISO VG32" or "ISO VG46" based on application. Thermodynamic properties of these working fluids are temperature dependent. Expressions, as a function of temperature, are used to calculate these properties. These expressions are derived by curve fitting of oil properties that are derived from extensive lab testing. Fluid heat transfer is solved using thermal energy equation with viscous dissipation included. Turbulence "shear stress transport" model with automatic wall function is employed when the flow is simulated as turbulent. Above turbulence setting enables the solver to capture laminar flow effects in viscous sublayers. In cases where the flow is simulated as laminar, turbulence model is turned off. The axis of rotation of the shaft moves as the bearing rotates. In CFX, expressions are defined to align the shaft axis with eccentricity at every position of the shaft.

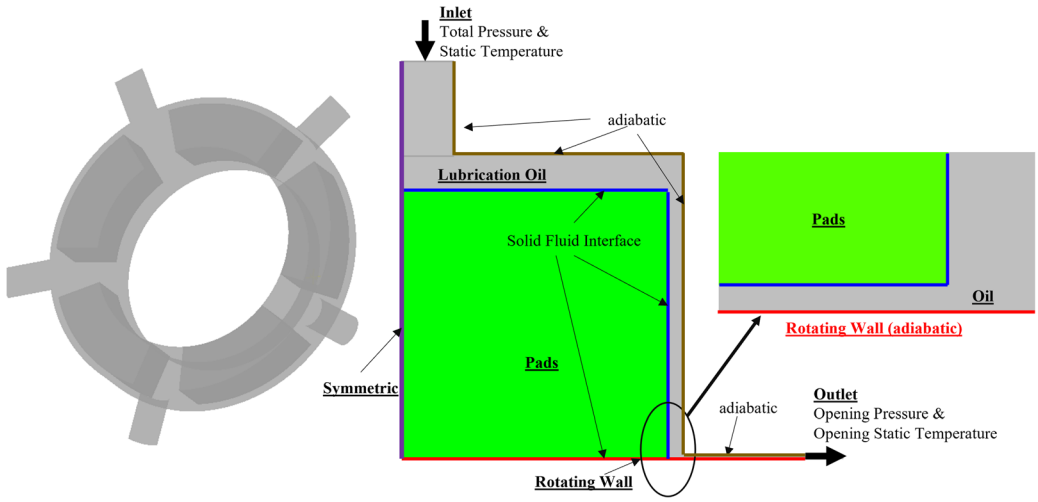

Fig. 6 Boundary conditions in CFX

The parameter set block in Fig. 4 contains all the input and output parameters of the three blocks of the CFD model. In this way, it is possible to change the inputs of the model and extract the most relevant outputs without the necessity to open the relative tools. For example, the geometry block receives as inputs the eccentricity of the shaft, the rotations of the pads and all the parameters that define both the microgeometry and macrogeometry of the bearing. For the ICEM CFD block, the inputs and outputs are related to the mesh size and quality. The inputs of CFX-pre are related to the operating conditions of the bearing. For example, the feeding pressure and temperature of the oil can be assigned together with the speed of the shaft and the load. As output, the torques of the pads and forces of the shaft are extracted. Moreover, the maximum temperature of the oil, maximum temperature of the pads, maximum temperature of each pad temperature probes, and outlet oil temperature are evaluated. The inlet and outlet oil flowrates are also relevant parameters for the investigation.

2.2 Newton–Raphson Equilibrium Position Search. The initial guess equilibrium position is estimated with the Reynolds based model in Ref. [7]. The tentative equilibrium position is defined as

$$\mathbf{p}^0 = \begin{bmatrix} \mathbf{z}^0 \\ \boldsymbol{\theta}^0 \end{bmatrix} \tag{1}$$

where $\mathbf{z}^0 = \begin{bmatrix} x^0 & y^0 \end{bmatrix}^T$ is the vector of shaft position and $\boldsymbol{\theta}^0 = \begin{bmatrix} \theta_1^0 & \theta_2^0 & \theta_k^0 & \dots & \theta_{N=5}^0 \end{bmatrix}^T$ is the vector containing the $N = 5$ pad rotations at the step 0. The initial equilibrium position is assigned to the CFD model and 250 CFD iterations are performed to stabilize the calculations of the pad torques $\mathbf{M}^0$ with respect to the pivot position and forces F_x^0, F_y^0. Then the new position vector $\mathbf{p}^1$ at step 1 is updated as

$$\mathbf{p}^1 = \begin{bmatrix} \mathbf{z}^0 \\ \boldsymbol{\theta}^1 = \boldsymbol{\theta}^0 + \Delta\boldsymbol{\theta} \end{bmatrix} \tag{2}$$

where $\Delta\theta$ is an infinitesimal rotation. Then, 50 CFD iterations are preformed to evaluate the new pad torques $\mathbf{M}^1$. Similarly, to the previous 250 CFD iterations, the 50 CFD iterations are sufficient to obtain converged values for the pad torques and shaft forces. The Jacobian of the torque for the kth pad is evaluated as

$$J_k = \frac{M_k^1 - M_k^0}{\Delta\theta} \tag{3}$$

The new pad equilibrium position $\mathbf{p}^2$, only related to the pad rotation, is calculated as

$$\mathbf{p}^2 = \begin{bmatrix} \mathbf{z}^0 \\ \boldsymbol{\theta}^2 \end{bmatrix} \tag{4}$$

where

$$\theta_k^2 = \theta_k^0 - \frac{M_k^0}{J_k}\eta \tag{5}$$

where η is a relaxation coefficient to avoid excessive pad rotation. Once $\mathbf{p}^2$ is obtained, 50 CFD iterations are performed to evaluate the values of the torques $\mathbf{M}^2$ and forces $\mathbf{F}^2$.

A similar approach is followed to evaluate the Jacobian of the forces related to the displacement of the shaft

$$\mathbf{p}^3 = \begin{bmatrix} \mathbf{z}^3 \\ \boldsymbol{\theta}^2 \end{bmatrix}, \mathbf{p}^4 = \begin{bmatrix} \mathbf{z}^4 \\ \boldsymbol{\theta}^2 \end{bmatrix} \tag{6}$$

where

$$\mathbf{z}^3 = \begin{bmatrix} x^0 + \Delta x \\ y^0 \end{bmatrix}, \quad \mathbf{z}^4 = \begin{bmatrix} x^0 \\ y^0 + \Delta y \end{bmatrix} \tag{7}$$

Δx and Δy are infinitesimal displacements of the shaft. Both $\mathbf{p}^3$ and $\mathbf{p}^4$ positions are simulated to obtain the variations of the forces $\mathbf{F}^3$ and $\mathbf{F}^4$. The force Jacobians are then calculated as

$$\begin{bmatrix} J_{xx} \\ J_{yx} \end{bmatrix} = \begin{bmatrix} \dfrac{F_x^3 - F_x^2}{\Delta x} \\ \dfrac{F_y^3 - F_y^2}{\Delta x} \end{bmatrix} \tag{8}$$

$$\begin{bmatrix} J_{xy} \\ J_{yy} \end{bmatrix} = \begin{bmatrix} \dfrac{F_x^4 - F_x^2}{\Delta y} \\ \dfrac{F_y^4 - F_y^2}{\Delta y} \end{bmatrix} \tag{9}$$

The new equilibrium position is then calculated as

$$\mathbf{p}^5 = \begin{bmatrix} \mathbf{z}^5 \\ \boldsymbol{\theta}^2 \end{bmatrix} \tag{10}$$

where

$$\mathbf{z}^5 = \mathbf{z}^2 + \begin{bmatrix} J_{xx} & J_{xy} \\ J_{yx} & J_{yy} \end{bmatrix}^{-1} \begin{bmatrix} F_x^2 - F_x^{\text{ref}} \\ F_y^2 - F_y^{\text{ref}} \end{bmatrix} \tag{11}$$

where F_x^{ref} and F_y^{ref} are the components of the bearing load in the horizontal and vertical directions. Then 50 CFD iterations are performed to evaluate the forces and torques for the new equilibrium position $\mathbf{p}^5$. The procedure is continued until the convergence on the expected shaft forces and pad torques at equilibrium are obtained. The equilibrium position is considered converged if the relative error between the shaft forces and pad torques calculated at two consecutives $\mathbf{p}^5$ is lower than 1%. After the equilibrium position is calculated, 250 CFD iterations are computed to guarantee the convergence of the monitored temperatures and flowrates, i.e., variation lower than 0.1%.

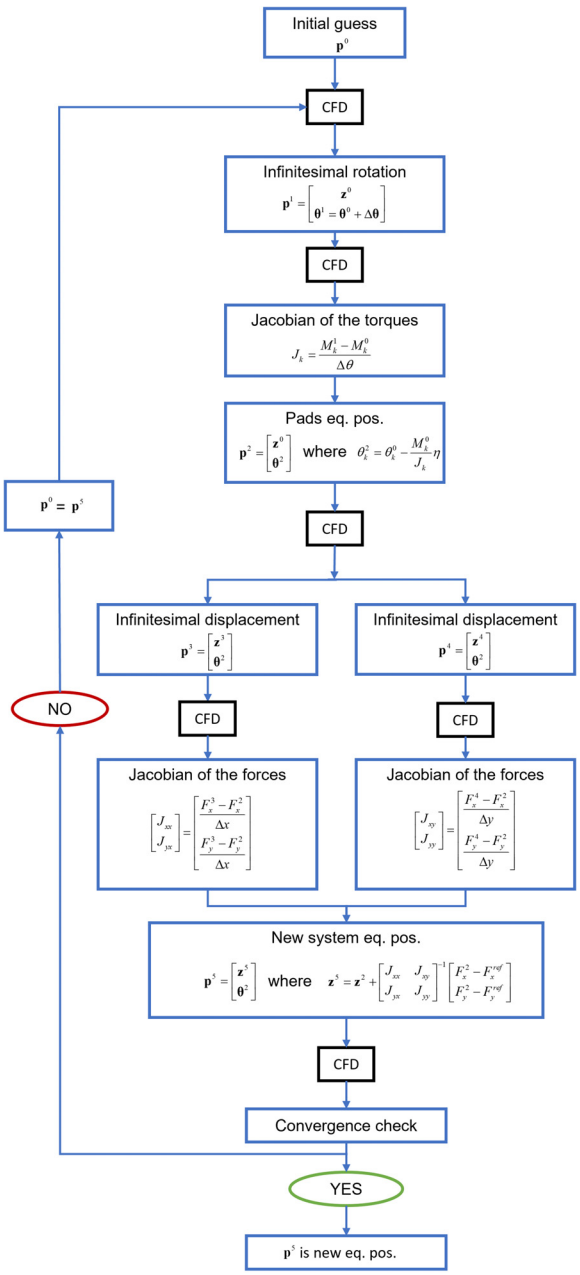

Fig. 7 Newton–Raphson algorithm for equilibrium search

The flowchart of the numerical procedure is represented in Fig. 7.

A similar approach is proposed in Ref. [14]. However, the Jacobians are only evaluated at the initial guess equilibrium position and kept constant during the whole calculation. In the model presented in this paper, the Jacobians calculation is performed every two loops to refine the procedure. The evolutions of the relevant quantities monitored during the equilibrium position search in the last step 5, are shown in Fig. 8.

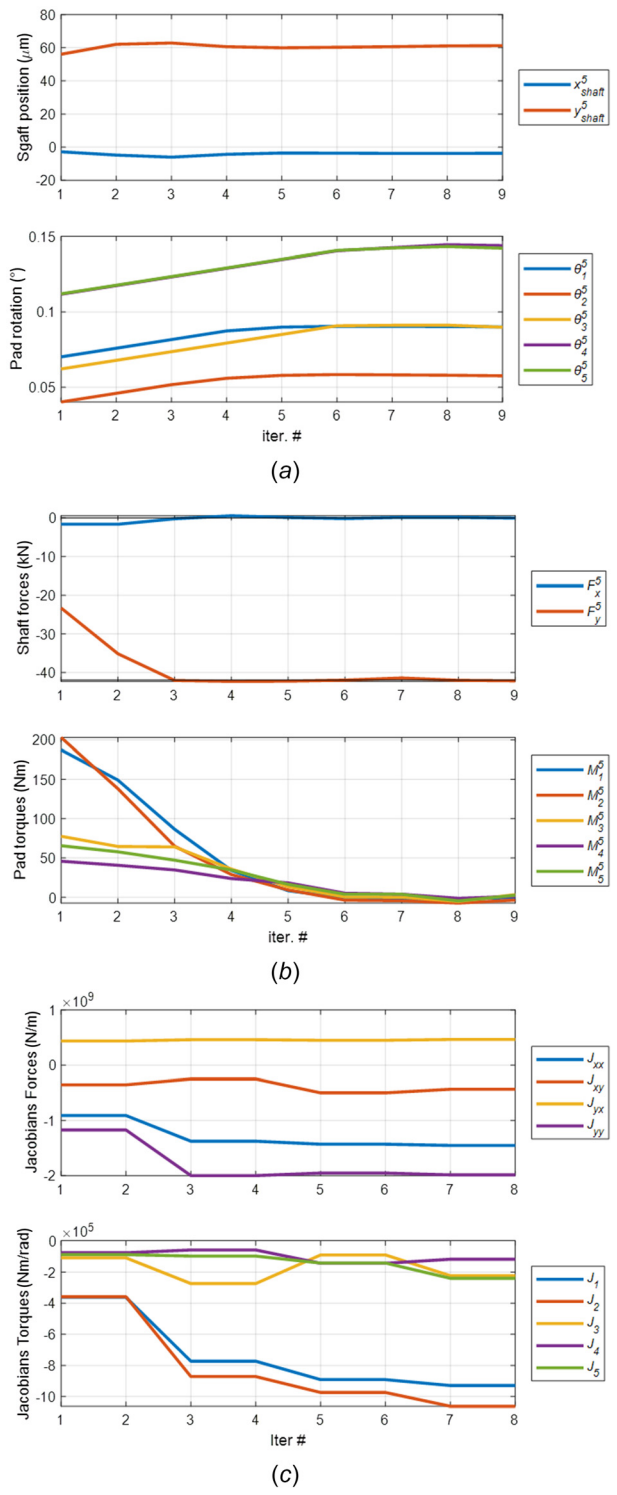

Fig. 8 Evolution of shaft position and pad rotations (*a*), shaft forces and pads torques (*b*), forces and torques evolution during equilibrium position search

2.3 Experimental Test Procedure. The experimental data considered for the validation of the numerical model are obtained from Mechanical Running Tests in compliance with American Petroleum Institute API 617 standards [18]. During this test, the mechanical operation of the machine is verified. The rotor vibration up to operating and trip speed is monitored together with bearing metal temperature. The monitoring system design is reported in API 670 standard [19]. During the test, bearing oil flow, inlet oil temperature, rotor speed, supply pressure, rotor vibrations, and metal temperature are continuously monitored. Temperature probes are installed on the two most loaded pads of the bearing at 75% of the pad arc from the pad leading edge and at 2.5 mm from the white metal surface, as prescribed by API 670 standard. The probe axial position is at roughly 20 mm from the pad external surface as shown in Fig. 2. The measurements of oil supply flowrate and pad temperature are taken as reference for the model validation. The shaft speed, inlet oil temperature, and supply pressure are input parameters.

3 Results and Discussion

In this section, test data are compared with numerical data. Test data are represented by a single horizontal line. A single value is obtained experimentally for each bearing size and operating conditions. The CFD analysis results are represented as the average considering the bearing with maximum and minimum tolerances of pads, bearing housing, shaft, and end seals. To take into consideration the measurements errors, the inlet flowrate is shown with a ±5% confidence bandwidth while the probe temperature is shown with a ±2 °C bandwidth.

3.1 Mesh Sensitivity. Mesh sensitivity analysis is carried out to check mesh dependency of the results. This study was carried out for the two bearing family extremes, namely, 80 mm and 200 mm bearing nominal diameters, Fig. 9. Across the bearing sizes, the cold gap between pad and shaft have comparable dimensions of the order of few tenths of a millimeter. Both the 80 mm and 200 mm meshes have been conceived with a constant number of nodes within the thin film gap. However, from this study, it was observed that increasing the number of nodes in this gap, from 15 nodes to 21 nodes, an improvement in flow and thermal behavior of the system was registered. In a later stage, the number of elements in other portions of the domain was also increased. Studies were also carried out with much wider range of meshes size across the domain. Only six mesh sizes are reported in Fig. 10. Beyond the mesh size that is labeled as "fine mesh" here, there was no significant change in flowrate and temperature predictions. Hence, the selected mesh ensures that the results are mesh independent. The mesh count of final models opted after the sensitivity study is shown in Fig. 9 for both the 80 mm and 200 mm bearings.

The sensitivity study improved the temperature and flow estimation. The numerical results are now closer to the experimental

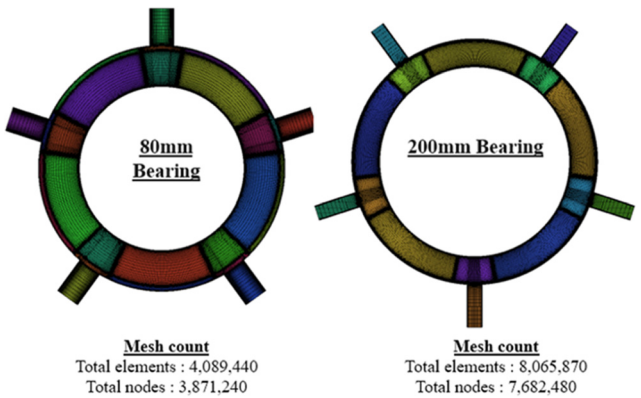

Fig. 9 Mesh and mesh count for 80 mm and 200 mm

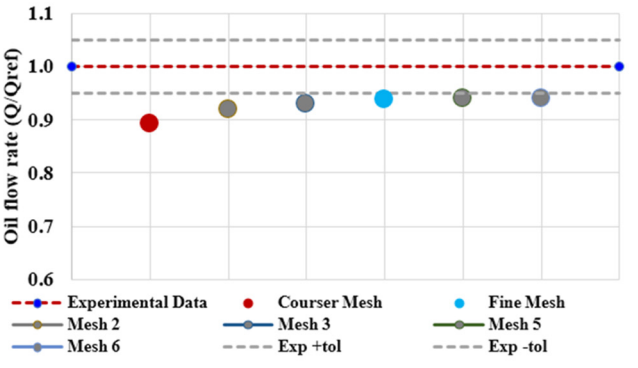

(*a*)

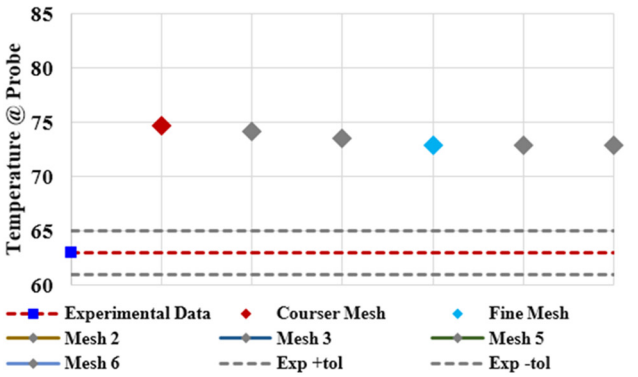

(*b*)

Fig. 10 Impact of mesh size on flowrate (*a*) and probe temperature and (*b*) estimations

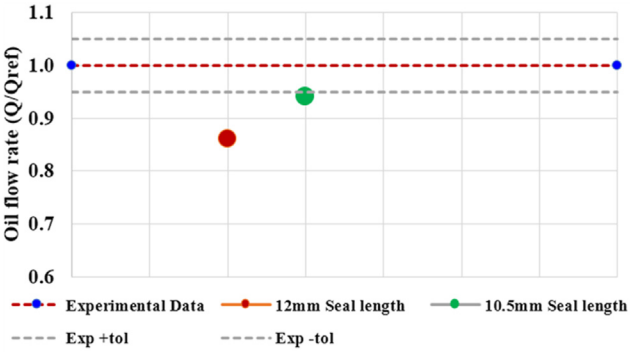

(*a*)

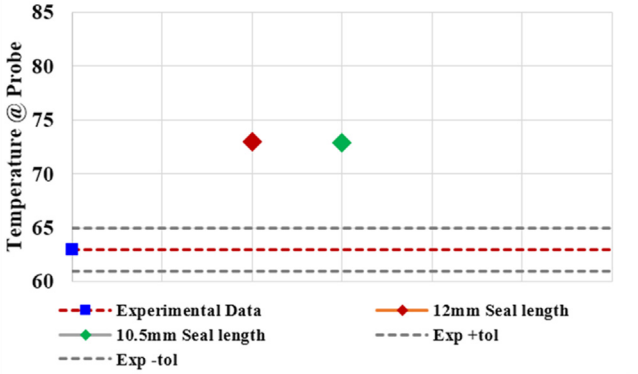

(*b*)

Fig. 11 Impact of seal length on flowrate (*a*) and probe temperature (*b*) estimations

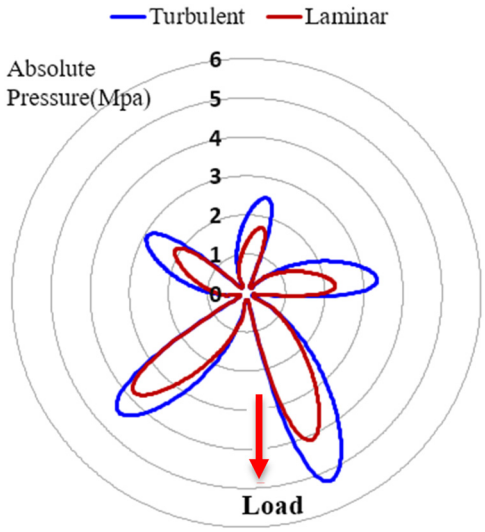

Fig. 12 Pressure distribution on pads for laminar versus turbulent cases

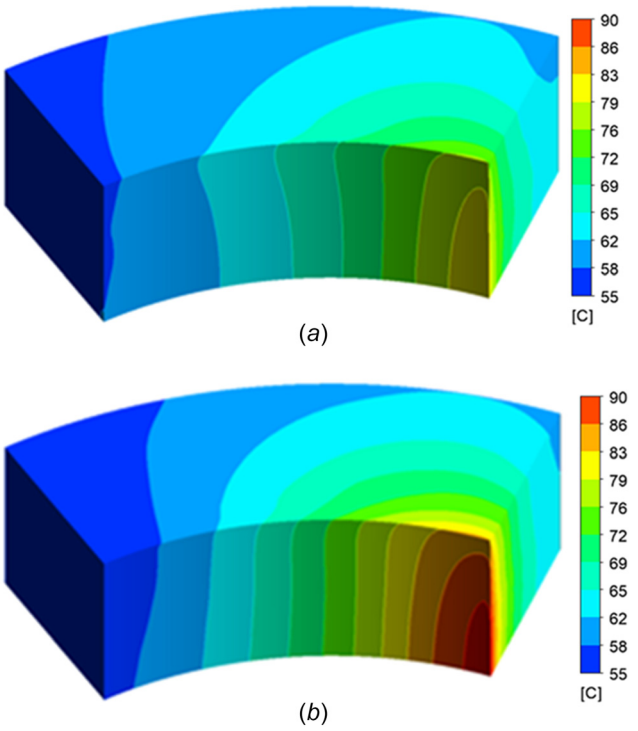

Fig. 13 Impact of turbulent (*a*) versus laminar (*b*) flow modeling on loaded pad temperatures. Only half pad is shown for the symmetry.

results as shown in Fig. 10 in which, for confidential reasons, the oil flowrate is normalized with respect to the reference oil flowrate. Laminar flow is considered for both the course mesh model and the fine mesh model.

3.2 Seal Length Effect. The amount of flow calculated by the model is sensitive to length of the seal. Since the pressure boundary condition is defined at the seal outlet, the length of the seal strongly determines the pressure distribution in the housing and the flow through the domain. The impact of a seal length change of 1.5 mm on the calculated flow is shown in Fig. 11(*a*). From Fig. 11(*b*), it can be observed that despite the change of flow there is a negligible impact on the temperatures at pad probe as most of this additional flow is bypassed from the thin film gaps and flows in the grooves between the pads. The results shown in Fig. 11 are obtained with the finer mesh model introduced in Sec. 3.1. Moreover, the flow is modeled considering the flow as laminar flow.

3.3 Laminar Versus Turbulent Modeling. In rotating machines working at high speed, the flow exhibits behavior that is between laminar and fully developed turbulence. This is called as "Superlaminar" condition [11]. A comparative study has been carried out, on 80 mm and 200 mm bearings. The flow is assumed either as fully laminar or turbulent. An accurate estimation of thermal and flow characteristics of a bearing is possible when pressure and temperatures are correctly estimated over the loaded face of the pads. Several studies [11] have established that accounting for low-recorrection in viscous sublayer is essential for a good estimation of turbulence effects. In current studies, the CFX shear stress transport option with automatic wall function is employed. The automatic near wall treatment automatically switches from wall function to low-remodel near walls. For this, it is recommended to have at least ten nodes within the thin gaps.

The pressure estimation for the turbulence modeling and laminar modeling is shown in Fig. 12. The laminar model predicts significantly lower pressures on the loaded pad surfaces than the turbulent one. The effect of the flow modeling on the pads surfaces temperatures is shown in Fig. 13 for the most loaded pad in the direction of the load and the 200 mm bearing. The laminar model predicts the maximum temperature 10 °C higher on the loaded surface. This results from the lower heat transfer between the oil and the pads in laminar modeling than in turbulent one.

Figure 14(*a*) shows that in both 80 mm and 200 mm bearings, laminar models predict higher flowrate through the bearings than

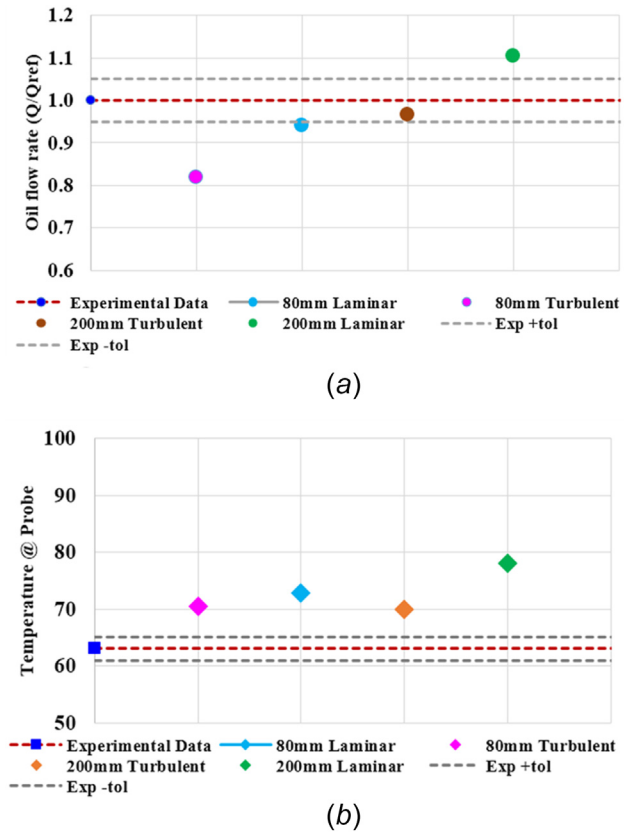

Fig. 14 Impact of laminar versus turbulent flow modeling on flowrate (*a*) and probe temperature (*b*)

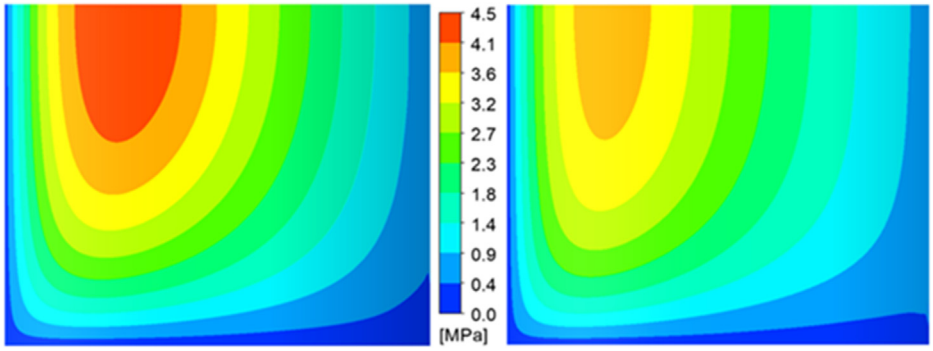

Fig. 15 80 mm most loaded surface absolute pressure distribution (laminar versus turbulent). Only half pad is shown for the symmetry.

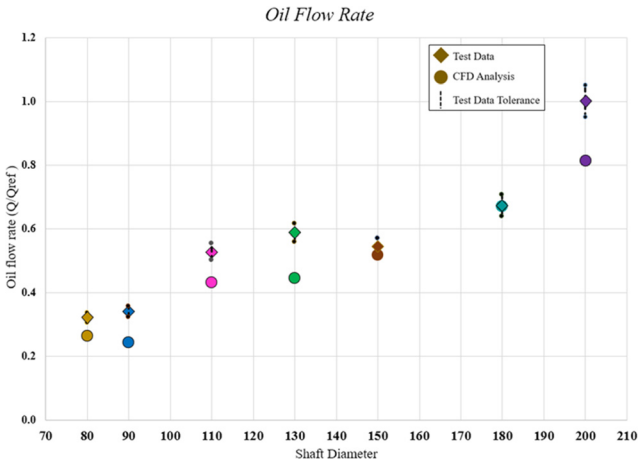

Fig. 16 Experimental and numerical flowrate comparison for different bearing sizes

the shear stress transport turbulence model. For the 80 mm bearing, the laminar modeling flowrate predictions are closer to the experimental value than the turbulent ones. On the contrary, for the 200 mm bearing, the turbulent modeling flowrate predictions are closer to the experimental result. The effect on the probe temperature of the flow modeling is shown in Fig. 14(*b*). In 200 mm bearing, the Reynolds number is double than that the 80 mm bearing. Therefore, a large discrepancy between the laminar and turbulent prediction can be observed. On the contrary, the Reynolds number of the 80 mm bearing is close to the laminar condition. Therefore, the difference in the probe temperature prediction of the laminar and turbulent models is minimal for the 80 mm bearing.

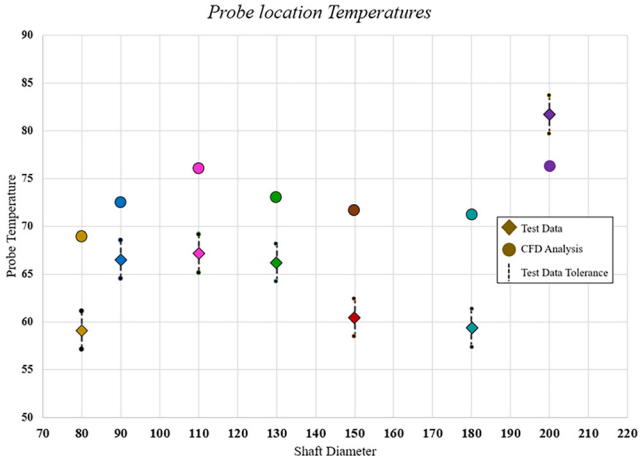

Fig. 17 Experimental and numerical probe temperature comparison for different bearing sizes

The pressure distributions on the surface of the most loaded pad obtained with the laminar and turbulent modeling are shown in Fig. 15. In both cases, the shape of the pressure profile is similar. However, the value of the maximum pressure changes significantly.

3.4 Bearing Family Analysis. The comparison between the numerical and experimental flowrate and temperatures for all the bearing diameters from 80 mm to 200 mm is shown in Figs. 16 and 17, respectively, in which the rhombus dot represents the data from test and the circular dot represents data from above described CFD analysis. *X*-axis has diameter for which data are plotted. Analysis for all these bearing sizes is performed considering turbulent flow. From Fig. 16, it can be noticed that for most of the bearings sizes the numerical results are in close agreement with the test results. For few bearings designs, the flow predicted is lower than the experimental one. These results are conservative with respect to the designer point of view. In case 180 mm bearing, there is an exact match between test and analysis data.

From Fig. 17, it can be noticed that except for the 200 mm bearing, temperature at the probe location is overestimated by analysis by about 2–8 °C. Higher temperature prediction by CFD can be considered as a conservative prediction, from designer perspective.

4 Conclusion

In this study, a 3D CFD model for TPJB is presented. The conjugate heat transfer between the pads and the oil is considered. The fully parametric construction of the geometry and meshing strategy allows to adopt the Newton–Raphson algorithm for the automatic calculation of the equilibrium condition. The effect of the mesh size, geometry, and flow modeling is investigated. The CFD model results are effective in predicting the static quantities of the bearing family investigated. Moreover, the parametric geometry and meshing strategy allow to avoid using a dynamic mesh algorithm, simplifying the modeling, and guaranteeing an optimal mesh quality throughout the equilibrium position calculation. The ability of above discussed CFD model, to be adaptable to all bearing sizes within the family, enables the designer to perform various design studies in less time and have more insight into performance of the design.

The proposed CFD model has been used to reduce the amount of oil flow in real work application in centrifugal compressors. Therefore, it represents an important tool for the reduction of the carbon footprint of TPJBs.

As a future development of the model, it is possible to consider a portion of the shaft to take into account the heat exchange between the oil film and the shaft itself. Moreover, adding the effect of the pivot flexibility and pad thermomechanical deformation can improve the accuracy of the predictions.

Acknowledgment

We thank Baker Hughes for funding the project. The rights of all figures are reserved to Baker Hughes Company.

Data Availability Statement

The datasets generated and supporting the findings of this article are obtainable from the corresponding author upon reasonable request.

Nomenclature

F_x^i, F_y^i = shaft forces at ith equilibrium search step
$F_x^{\text{ref}}, F_y^{\text{ref}}$ = reference shaft forces at equilibrium
J_k = Jacobian of kth pad torque
J_{xy} = force Jacobian
$\mathbf{p}^i$ = equilibrium position vector at ith step
x^i = shaft horizontal position at ith step
y^i = shaft vertical position at ith step
$\boldsymbol{\theta}^i$ = pad rotation vector at ith step

References

[1] Lund, J. W., 1964, "Spring and Damping Coefficients for the Tilting-Pad Journal Bearing," ASLE Trans., **7**(4), pp. 342–352.
[2] Tieu, A. K., 1973, "Oil-Film Temperature Distribution in an Infinitely Wide Slider Bearing: An Application of the Finite-Element Method," J. Mech. Eng. Sci., **15**(4), pp. 311–320.
[3] Knight, J. D., and Barrett, L. E., 1988, "Analysis of Tilting Pad Journal Bearings With Heat Transfer Effects," ASME J. Tribol., **110**(1), pp. 128–133.
[4] Kim, J., Palazzolo, A. B., and Gadangi, R. K., 1994, "TEHD Analysis for Tilting-Pad Journal Bearings Using Upwind Finite Element Method," Tribol. Trans., **37**(4), pp. 771–783.
[5] Suh, J., and Palazzolo, A., 2015, "Three-Dimensional Dynamic Model of TEHD Tilting-Pad Journal Bearing—Part I: Theoretical Modeling," ASME J. Tribol., **137**(4), p. 041703.
[6] Chatterton, S., Pennacchi, P., Vania, A., de Luca, A., and Dang, P. V., 2019, "Tribo-Design of Lubricants for Power Loss Reduction in the Oil-Film Bearings of a Process Industry Machine: Modelling and Experimental Tests," Tribol. Int., **130**, pp. 133–145.
[7] Chatterton, S., Pennacchi, P., Vania, A., and Dang, P. V., 2019, "Cooled Pads for Tilting-Pad Journal Bearings," Lubricants, **7**(10), p. 92.
[8] Yang, J., and Palazzolo, A., 2021, "Computational Fluid Dynamics Based Mixing Prediction for Tilt Pad Journal Bearing TEHD Modeling—Part II: Implementation With Machine Learning," ASME J. Tribol., **143**(1), p. 011802.
[9] Yang, J., and Palazzolo, A., 2021, "Computational Fluid Dynamics Based Mixing Prediction for Tilt Pad Journal Bearing TEHD Modeling—Part I: TEHD-CFD Model Validation and Improvements," ASME J. Tribol., **143**(1), p. 011801.
[10] Yang, J., and Palazzolo, A., 2022, "Deep Convolutional Autoencoder Augmented CFD Thermal Analysis of Bearings With Inter Pad Groove Mixing," Int. J. Heat Mass Transfer, **188**, p. 122639.
[11] Ding, A., Ren, X., Li, X., and Gu, C., 2018, "Numerical Investigation of Turbulence Models for a Superlaminar Journal Bearing," Adv. Tribol., **2018**, pp. 1–14.
[12] Armentrout, R. W., He, M., Haykin, T., and Reed, A. E., 2017, "Analysis of Turbulence and Convective Inertia in a Water-Lubricated Tilting-Pad Journal Bearing Using Conventional and CFD Approaches," Tribol. Trans., **60**(6), pp. 1129–1147.
[13] Hagemann, T., Zeh, C., and Schwarze, H., 2019, "Heat Convection Coefficients of a Tilting-Pad Journal Bearing With Directed Lubrication," Tribol. Int., **136**, pp. 114–126.
[14] Yang, J., and Palazzolo, A., 2019, "Three-Dimensional Thermo-Elasto-Hydrodynamic Computational Fluid Dynamics Model of a Tilting Pad Journal Bearing—Part I: Static Response," ASME J. Tribol., **141**(6), p. 061702.
[15] Yang, J., and Palazzolo, A., 2019, "Three-Dimensional Thermo-Elasto-Hydrodynamic Computational Fluid Dynamics Model of a Tilting Pad Journal Bearing—Part II: Dynamic Response," ASME J. Tribol., **141**(6), p. 061703.
[16] Li, M., Gu, C., Pan, X., Zheng, S., and Li, Q., 2016, "A New Dynamic Mesh Algorithm for Studying the 3D Transient Flow Field of Tilting Pad Journal Bearings," Proc. Inst. Mech. Eng., Part J, **230**(12), pp. 1470–1482.
[17] Andrés, L. S., and Li, Y., 2015, "Effect of Pad Flexibility on the Performance of Tilting Pad Journal Bearings-Benchmarking a Predictive Model," ASME J. Eng. Gas Turbines Power, **137**(12), p. 122503.
[18] American Petroleum Institute, 2014, "Standard–Axial and Centrifugal Compressorsand Expander-Compressors for Petroleum, Chemical and Gas Industry Services," API 617, 8th Edition, American Petroleum Institute, Washington, DC.
[19] American Petroleum Institute, 2014, "API 670 Standard—Machinery Protection System," American Petroleum Institute (API), Washington, DC.